

Manuscript version: Author's Accepted Manuscript

The version presented in WRAP is the author's accepted manuscript and may differ from the published version or Version of Record.

Persistent WRAP URL:

<http://wrap.warwick.ac.uk/160740>

How to cite:

Please refer to published version for the most recent bibliographic citation information. If a published version is known of, the repository item page linked to above, will contain details on accessing it.

Copyright and reuse:

The Warwick Research Archive Portal (WRAP) makes this work by researchers of the University of Warwick available open access under the following conditions.

Copyright © and all moral rights to the version of the paper presented here belong to the individual author(s) and/or other copyright owners. To the extent reasonable and practicable the material made available in WRAP has been checked for eligibility before being made available.

Copies of full items can be used for personal research or study, educational, or not-for-profit purposes without prior permission or charge. Provided that the authors, title and full bibliographic details are credited, a hyperlink and/or URL is given for the original metadata page and the content is not changed in any way.

Publisher's statement:

Please refer to the repository item page, publisher's statement section, for further information.

For more information, please contact the WRAP Team at: wrap@warwick.ac.uk.



The Effect of Organic Cation Dynamics on the Optical Properties in (PEA)₂(MA)[Pb₂I₇] Perovskite Dimorphs

Journal:	<i>Journal of Materials Chemistry C</i>
Manuscript ID	TC-ART-09-2021-004181
Article Type:	Paper
Date Submitted by the Author:	03-Sep-2021
Complete List of Authors:	Yulia, Lekina; Nanyang Technological University, Division of Physics and Applied Physics, School of Physical and Mathematical Sciences; Dintakurti, Sai; Nanyang Technological University, Interdisciplinary Graduate School; University of Warwick, Physics Febriansyah, Benny; Nanyang Technological University, Energy Research Institute @ Nanyang Technological University Bradley, David; University of Warwick Yan, Jiaxu; Nanjing Tech University (NanjingTech), Institute of Advanced Materials Shi, Xiangyan; Nanyang Technological University, Division of Physics and Applied Physics, School of Physical and Mathematical Sciences England, Jason; Nanyang Technological University, School of Physical and Mathematical Sciences White, T.; ntu, Hanna, John; University of Warwick, Department of Physics Shen, Zexiang; Nanyang Technological University, School of Physical and Mathematical Sciences

The Effect of Organic Cation Dynamics on the Optical Properties in (PEA)₂(MA)[Pb₂I₇] Perovskite Dimorphs

Received 00th January 20xx,
Accepted 00th January 20xx

Yulia Lekina,^{a,b} Sai S.H. Dintakurti,^{c,d} Benny Febriansyah,^e D.J. Bradley,^d Jiaxu Yan,^f Xiangyan Shi,^b Jason England,^e Tim White,^g John V. Hanna,^{*d,g} Ze Xiang Shen^{*a,b}

DOI: 10.1039/x0xx00000x

Two-dimensional (2D) phenylethyl ammonium (PEA⁺)-methyl ammonium (MA⁺) lead iodide ((PEA)₂(MA)[Pb₂I₇]) hybrid perovskite exists as temperature-dependent dimorphs exhibiting an ill-defined phase transition occurring over 150 - 200 K range. Raman scattering, photoluminescence, optical absorbance and solid state MAS NMR spectroscopic methods are employed to investigate the structural complexity, disorder and structure/function of this system. The Raman and ¹H MAS NMR data indicate that the lower bounds of the phase transition at ~150 K is characterised by attenuated rotational modes and slower motional dynamics throughout the disordered MA⁺ organic sublattice, inducing a strengthening of the MA⁺...I hydrogen bonds and a 5 meV increase in the excitonic and photoluminescence energies. It is evident that different recombination mechanisms are dominant for the room temperature and low temperature phases reflecting the importance of MA⁺ dynamics in the optical properties of the material. Single crystal X-ray studies are unable to position the organic cations within the Pb₂I₇ framework; however, ¹H/¹³C MAS NMR measurements describe elements of local structural disorder based on conformational isomerism within the PEA⁺ sublattice. Concomitant I⁻ and Pb²⁺ migration and [Pb₂I₇]³⁻ framework defects create stacking disorder, dislocations and dispersed octahedral tilting leading to additional disorder and distributed MA⁺ and PEA⁺ cation dynamics.

Introduction

Hybrid organic-inorganic halide perovskites have attracted intense attention due to their high performance and low cost for light harvesting applications.^{1–3} These materials can also be deployed as light emitting diodes (LEDs),^{1,4,5} X-ray and photo detectors^{6,7}, spintronics⁸ and lasing applications.⁹ The solar cell performance of AMX₃ perovskites (A is an organic cation, usually MA = CH₃-NH₃⁺, M = Pb, Sn, X = I, Br, Cl or a mixture of them) has evolved much faster than other photovoltaic materials,^{1,10} with a power conversion efficiency (PCE) of more than 25% being achieved.^{11–13} However, poor moisture stability and degradation of the photoluminescence characteristics remain as significant obstacles to the fabrication of low-cost and long lifetime devices from 3D hybrid perovskite systems^{1,8}. In comparison, 2D perovskites have demonstrated improved stability and flexible chemical engineering possibilities for solar light-harvesting and LED applications^{8,14–18}. These materials have been found to be excellent candidates for light emitting diode (LED) applications due to tenability, high quantum efficiencies, and broadband emission^{8,14–19}.

The crystal structures of 2D perovskites are derived from the cubic perovskite aristotype by slicing on the {100} planes and intercalating organic cations to yield a layered structure with corner-sharing MX₆ octahedral blocks occupying the basal plane (Fig. 1). This yields the general formula R₂(A)_{n-1}M_nX_{3n+1}, where R is the long organic cation-spacer, A is a small organic (or inorganic) cation such as methylammonium (MA⁺), and n indicates the number of octahedral layers within each inorganic block.²⁰ Introducing hydrophobic organic layers simultaneously provides protection from moisture and creates intrinsic quantum wells that widens the band gap and promotes strong excitonic properties due to quantum confinement.^{21–24}

In general, the typical architecture of 2D hybrid perovskite systems relies on the electronic structure being directly controlled by the inorganic sublattice, while the organic cations provide more subtle steric influences.^{20,22,25} Previous work has reported that the top of the valence band is influenced by the Pb 6s and I 5p orbitals, while conversely the bottom of the conduction band by Pb 6p and I 5s orbitals.²⁵ In particular, the Pb-I bond length within the PbI₆ octahedron and Pb-I-Pb bridging angle between PbI₆ octahedra correlate closely with the electronic structure and optical properties.^{22,26,27} Consequently, temperature driven polymorphism leads to abrupt changes in optical and electronic properties, and device

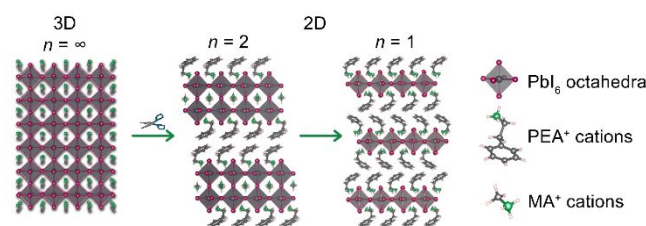


Fig. 1 Generalized scheme of the crystal structure types comprising 2D perovskite systems.

^a Centre for Disruptive Photonic Technologies, Nanyang Technological University, 637371, Singapore.

^b Division of Physics and Applied Physics, School of Physical and Mathematical Sciences, Nanyang Technological University, 637371, Singapore.

^c Interdisciplinary Graduate School (IGS), Nanyang Technological University, 50 Nanyang Avenue, Singapore 639798, Singapore.

^d Department of Physics, University of Warwick, Gibbet Hill Rd., Coventry CV4 7AL, UK

^e Division of Chemistry and Biological Chemistry, School of Physical and Mathematical Sciences, Nanyang Technological University, 21 Nanyang Link, Singapore 637371, Singapore.

^f Key Laboratory of Flexible Electronics (KLOFE) & Institute of Advanced Materials (IAM), Jiangsu National Synergistic Innovation Center for Advanced Materials (SICAM), Nanjing Tech University (Nanjing Tech), Nanjing 211816, China.

^g School of Materials Science and Engineering, Nanyang Technological University, 50 Nanyang Avenue, Singapore 639798, Singapore

Electronic Supplementary Information (ESI) available: [Supporting figures with structural information, additional NMR and optical spectroscopic data, pdf]. See DOI: 10.1039/x0xx00000x

performance, in these materials. For example, the 2D perovskite $(\text{PEA})_2[\text{PbI}_4]$ ($n = 1$, PEA = phenylethyl ammonium) system is structurally stable over a 10 - 340 K temperature range;^{28,29} however, in contrast the 3D perovskite system MAPbI_3 ($n = \infty$) undergoes two phase transitions over similar temperature ranges.³⁰ Furthermore, hydrogen bonding between the methylammonium cations was shown to be extremely important in 3D perovskites as this significantly increases the overall stability, and provides possibilities for tuning of the electronic states.^{31–34}

The 2D ($n = 2$) perovskite system $(\text{PEA})_2(\text{MA})[\text{Pb}_2\text{I}_7]$ is intermediate to MAPbI_3 and $(\text{PEA})_2[\text{PbI}_4]$, and it possesses MA^+ and PEA^+ cations which are both capable of forming hydrogen bonds. Substantial ambiguity and uncertainty surrounds the complete ambient and low temperature single crystal structure determinations of the $(\text{PEA})_2(\text{MA})[\text{Pb}_2\text{I}_7]$ system as the light elements are essentially invisible to the XRD technique.^{35,36} It is postulated that structural disorder throughout the organic substituents is responsible for the disorder, although this is yet to be established conclusively.³⁶ This uncertainty precludes an understanding of the low temperature photophysical properties,³⁷ and consequently the influence of hydrogen bonding in this process has not been thoroughly investigated. Raman spectroscopy has been demonstrated to be a very sensitive probe for studying hydrogen atom vibrational modes in hybrid perovskite systems, with recent studies characterizing the vibrational interactions between the MA^+ cation and halogen atoms in 3D perovskites.^{31,38}

This study describes a low temperature Raman spectroscopic investigation of the N-H bond vibrations, particularly those related to the formation of N-H...I hydrogen bonds in $(\text{PEA})_2(\text{MA})[\text{Pb}_2\text{I}_7]$, to provide complementary information to single crystal X-ray diffraction where lighter elements evade detection. The absorption, emission and Raman vibrational modes of $(\text{PEA})_2(\text{MA})[\text{Pb}_2\text{I}_7]$ over the 80 - 293 K temperature range have been analyzed, with a correlation of the MA^+ cation vibrations and excitonic features revealing a broad phase transition occurring over a wide temperature of range between 150 - 200 K. This study also utilizes solid state ^1H and ^{13}C MAS NMR to investigate and constrain the structural disorder that influences the organic PEA^+ and MA^+ cations, and shows that the broad phase transition could be attributed to gradual thermal rearrangement of the stacking disorder of the PEA^+ cations within the 2D interplanar channels, which also concomitantly disrupts the hydrogen bonding network.

Experimental

Synthesis

The synthesis procedure described previously by Stoumpos *et al.*²¹ was used to obtain crystalline $(\text{PEA})_2(\text{MA})[\text{Pb}_2\text{I}_7]$, however, the method was modified to include an excess of methyl ammonium iodide. Inorganic lead iodide (99.999%, trace metals

basis, perovskite grade), phenyl ethyl amine (99%), 57% w/w non-stabilized aqueous HI solution, and 50% aqueous H_3PO_2 were obtained from Sigma Aldrich, while methyl ammonium iodide was purchased from Dyesol. These reagents were used without purification unless otherwise stated in the associated procedure.

Phenyl ethyl ammonium iodide was prepared by slowly mixing the amine with a stoichiometric amount of hydroiodic acid in ethanol at 0 °C for 1 hour, after which the solvents were removed by rotary vacuum evaporation at 50 °C. Where necessary, excess ethanol was added to form an azeotropic mixture with water to remove the latter completely. The solid product was washed with diethyl ether to remove the remaining iodides. Finally, the ammonium salt was dried under vacuum at 50 °C overnight (1.76g; 83% yield). ^1H NMR (400 MHz, DMSO-d_6): δ 7.78 (bs, 3 H, NH_3), 7.32-7.20 (m, 5 H, ArH), 3.06-3.03 (m, 2 H, CH_2), 2.88-2.84 (m, 2 H, CH_2). $^{13}\text{C}\{^1\text{H}\}$ NMR (100 MHz, DMSO-d_6): δ 137.1, 128.6, 128.6, 126.7, 40.0, 32.8.

Then $(\text{PEA})_2(\text{MA})[\text{Pb}_2\text{I}_7]$ ($n = 2$) was prepared. A two-necked round bottom flask was used to combine PbI_2 powder (230 mg, 0.5 mmol), methyl ammonium (53 mg, 0.33 mmol) and phenyl ethyl ammonium iodide salts (125 mg, 0.5 mmol) with magnetic stirring. Methyl ammonium iodide was added with 30% excess. Subsequently, 57% w/w aqueous HI solution (2.0 mL) and 50% aqueous H_3PO_2 (0.20 mL) were added sequentially in a dropwise manner. The suspension was brought to reflux under flowing N_2 with continuous stirring (30 - 60 mins) to yield a clear, bright yellow solution. Stirring was discontinued and the solution cooled slowly to room temperature while red rectangular plates precipitate. The crystals were finally isolated by vacuum filtration, washed with copious amounts of diethyl ether, and thoroughly dried under vacuum for several hours.

Solid State ^{13}C and ^1H MAS NMR:

All solid-state MAS NMR measurements were acquired at 18.8 T using a Bruker Avance III-800 spectrometer operating at ^1H and ^{13}C Larmor frequencies of 800.16 and 201.19 MHz, respectively. These measurements were undertaken using a Bruker 0.7 mm triple channel H/C/N ultrafast MAS probe which enabled a MAS frequency of 110 kHz throughout this study. The ^1H MAS NMR data were acquired using single pulse methods which utilised a $\pi/2$ pulse length of 1.0 μs (calibrated using adamantane) and a recycle delay of 30 s. In contrast, the ^1H - ^{13}C cross-polarisation (CP) MAS NMR data were measured using an initial ^1H $\pi/2$ pulse time of 1.0 μs , a Hartmann-Hahn contact period (in the form of a CP ramp) of 2 ms, in conjunction with ^1H decoupling fields of >100 kHz during data acquisition. Both ^1H and ^{13}C chemical shifts were both referenced against TMS as the primary IUPAC reference ($\delta_{\text{iso}} = 0.0$ ppm) via a secondary solid adamantane reference ($\delta_{\text{iso}} = 1.9$ ppm for ^1H ; $\delta_{\text{iso}} = 37.7$ ppm for ^{13}C). The ^1H MAS NMR data were accurately simulated using the DMFit NMR software package to quantitatively estimate the relative proportions of the individual PEA^+ and MA^+ cations present.

Two-dimensional heteronuclear ^1H - ^{13}C correlation data was achieved through the use of the inversely detected hCH HETCOR experiment utilising forward ^{13}C - ^1H CP, evolution of the ^{13}C magnetisation under fast MAS and high ^1H decoupling conditions, and then reverse ^{13}C - ^1H CP for detection of the ^1H magnetisation. The preparatory ^1H and ^{13}C $\pi/2$ pulse lengths prior to the forward and reverse CP processes were both 1 μs in duration, while the forward and reverse CP ramps (contact periods) were both 2 ms. The 2D homonuclear ^1H - ^1H NOESY data were acquired using mixing times of 100 and 300 ms, a recycle delay of 5 s, with each experiment acquiring 160 slices in the indirect F1 dimension. The 2D homonuclear ^1H - ^1H single quantum-double quantum BABA recoupling experiment was performed using a single rotor synchronised recoupling loop of 9.1 μs , a double quantum evolution period of 15 μs , with 1280 slices comprising the indirect F1 dimension. All data were processed using the Bruker TopSpin (v 4.0.8) NMR data processing package. The ^1H T_1 relaxation times were measured using a saturation-recovery experiment. An initial pulse train of 100 $\pi/2$ pulses with a separation delay of 50 ms was used to achieve complete saturation prior to single pulse acquisition. The resulting data were deconvoluted and integrated using Dmfit simulation program.³⁹ The resulting integrated intensity data from each ^1H resonance was fitted with a single exponential function using OriginPro (2019) software to obtain the ^1H T_1 (spin-lattice) relaxation times.

Optical Characterization

A WITec Alpha 300RAS confocal Raman microscope was used to record Raman, photoluminescence (PL) and optical absorption spectra. The 633 nm (red) line from an 8 mW He-Ne gas laser coupled to an Acton spectrometer with a diffraction grating of 1800 grooves/mm (1.3 cm^{-1} resolution) and a thermoelectrically cooled Andor CCD detector was chosen to avoid photoluminescence. The backscattered Raman signal passed through two 633 nm BraggGrate Notch Filters (BNF) for effective laser line rejection. The blue line of a linearly polarized CW solid laser (457 nm) was chosen for PL measurements with the excitation power maintained below 0.8 μW to avoid detector photo-degradation and saturation. A halogen lamp (15 V, 150 W, 3100 K) served as the white light source for the absorption measurements. A long working distance 20 \times microscope objective (spot size of $\sim 2 \mu\text{m}$) was used for the low temperature experiments. All data were measured between 293 K and 78 K using a nitrogen gas flow cryostat.

Powder and Single Crystal X-ray Diffraction

Laboratory powder X-ray diffraction data were measured using a Shimadzu XRD-600040 diffractometer in θ - 2θ scan mode with a measurement rate of 1 degree/min. $\text{Cu-K}\alpha$ (1.5406 \AA) X-ray line was chosen as a source while using scintillation NaI detector. Single crystal X-ray diffraction data were collected on a Bruker X8 CCD diffractometer using a graphite-monochromated $\text{Mo-K}\alpha$ source ($\lambda = 0.71073 \text{ \AA}$) equipped with a CCD detector at room temperature. A full sphere collection was undertaken ranging from 2.325° to 29.000° . A total of 9178 reflections were observed of which 7388 had an intensity above

the threshold limit of $I > 2\sigma(I)$; these reflections were used to fit the structural model in the $P1$ triclinic space group. Data reduction and absorption corrections were performed with SAINT and SADABS respectively. The motif of the inorganic sublattice was determined by direct methods and refined by full-matrix least-squares procedures on F^2 using the Bruker SHELXL-2018 package. The location of the organic MA^+ and PEA^+ moieties could not be determined.

DFT Computation

First principle calculations, including atomic structure optimization, band structure and phonon frequencies simulation, were based on the Density Functional Theory (DFT). The Vienna *Ab initio* Simulation Package (VASP) code was used, employing the previously reported crystal structure³⁵ as the initial parameters. The exchange correlation potential was described using the Perdew, Burke and Ernzerhof (PBE) functional within the generalized gradient approximation (GGA).⁴⁰ The Brillouin zone was sampled by a $3 \times 3 \times 1$ k-point mesh using Monkhorst-Pack (MP) method. The energy convergence for the relaxation was chosen to be less than 10^{-5} eV/\AA . The newly developed vdW density functional (vdW-DF2) was deployed to account for nonlocal van der Waals interactions⁴¹.

Results and Discussion

Structural Characterization

ARTICLE

Journal Name

The formation of the 2D ($n = 2$) $(\text{PEA})_2(\text{MA})[\text{Pb}_2\text{I}_7]$ phase was confirmed by powder XRD analysis of the horizontally oriented platelets shown in Fig. S1. These data exhibit reflections that are consistent with results previously reported by Peng *et al.*⁴² An additional single crystal X-ray structure determination was conducted in order to obtain the accurate atomic coordinates. A partial structural solution with only the Pb and I atoms being located resulted in an unusually high R_1 value of 0.13 and Goof of 2.44. The refined lattice parameters, positional coordinates and equivalent isotropic displacement parameters are reported in Fig. S2 and Table S1. The organic atoms could not be located due to disorder in the organic sublattice. The highest q peak with an intensity of 13 electrons occurs at a distance of 1.69 Å from PB1 site. Splitting the PB1 site reduces the site occupancy factor by ~5%. Similarly, I5 has a q peak at a distance of 1.65 Å having an intensity corresponding to ~4%. The distance of 1.7 Å is lesser than the Pb-I bond distance of >3.1 Å, excluding the possibility of a presence of another atom so close to PB1 site. Detection of positional disorder at Pb and I sites with a distance of 1.7 Å in the same direction strongly suggests the presence of stacking dislocations at the 4 - 5% level. Stacking dislocations within the inorganic sublattice are attributed to the positional and conformational disorder in the organic sublattice accommodating the MA^+ and PEA^+ cations. The I and Pb Ueq values in Table S1 range from 0.053 - 0.063 Å³ and 0.0336 - 0.0334 Å³, respectively, indicating that the halogen atoms are comparatively more disordered. From Fig. S2, positions I8 and I9 protruding perpendicularly out of the PbI_6 plane exhibit the highest displacements, suggesting that this positional irregularity in the I species defining the interplanar channels is directly associated with the disorder perturbing the organic sublattice.

A characterisation of the disorder within the organic sublattice can be achieved using high resolution solid state ^1H and ^{13}C MAS NMR which is very sensitive to the short-range chemical environment defining each atomic species. Fig. 2 shows the ^1H ultra-fast MAS NMR data ($\nu_r = 110$ kHz) from the $(\text{PEA})_2(\text{MA})[\text{Pb}_2\text{I}_7]$ system presented with the spectral simulation and deconvolution, and the assigned ^1H chemical shifts representing the aromatic, amine and aliphatic moieties are summarized in Table 1. These data were acquired under fully relaxed conditions thus allowing a quantitative estimate of the H speciation. As observed from the ^1H shift assignments in Table 1, a quantitative simulation of the ^1H MAS NMR spectrum in Fig. 2 can be preserved only when a distribution of chemical shifts is introduced for the methylene positions 5 and 6. These

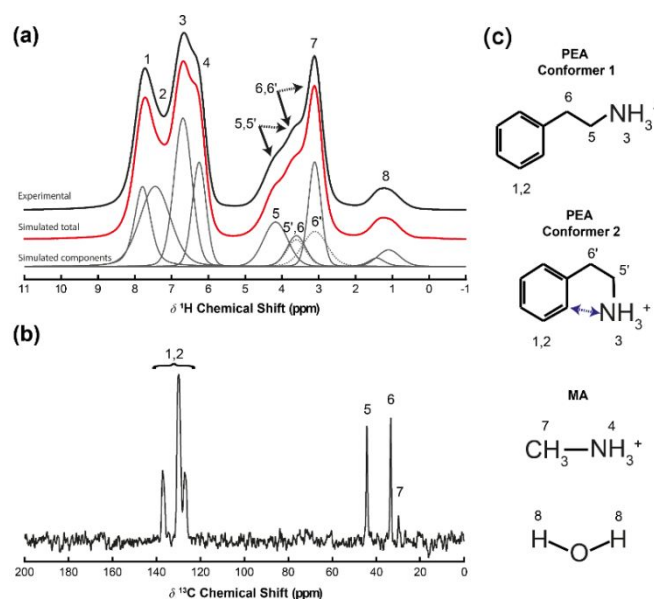


Fig. 2 1D solid state NMR data from the 2D ($n = 2$) $(\text{PEA})_2(\text{MA})[\text{Pb}_2\text{I}_7]$ system showing the (a) ^1H MAS NMR spectrum, deconvolution and assignments, (b) ^{13}C MAS NMR spectrum, acquired under high-field/ultra-fast MAS conditions ($\nu_{0,1\text{H}} = 800.16$ MHz, $\nu_{0,13\text{C}} = 201.19$ M

assignments were corroborated by the 2D heteronuclear and homonuclear MAS NMR data exhibited in Fig. 3. The 2D ^1H - ^{13}C hCH HETCOR data displayed in Fig. 3(a) shows the basic heteronuclear correlations expected for the aromatic, amine and aliphatic species comprising the PEA^+ and MA^+ cations. However, an expansion of the ^1H and ^{13}C aliphatic special regions (see Fig. 3(b)) indicates that the broader ^1H correlations are associated with both the α -CH₂ (H position 5) and β -CH₂ (H position 6) clearly span two well-defined H chemical environments. As represented in Fig. 2 and 3(b), it can be deduced that positional disorder characterizing the ethylamine side chain distributes the ^1H intensity from the α -CH₂ moiety between H positions 5 and 5'; similarly, the ^1H intensity from the β -CH₂ moiety is distributed between the H positions 6 and 6'. From the ^1H chemical shift assignments presented in Table 1, it is inferred that this rationalisation results in a $\text{PEA}^+:\text{MA}^+$ cation ratio of ~2:1 which is consistent with the nominal $(\text{PEA})_2(\text{MA})[\text{Pb}_2\text{I}_7]$ compositional stoichiometry.

The ^1H ultra-fast MAS NMR data of Fig. 2(a) and S3(a) also indicates the presence of structural H_2O evidenced by the broad upfield resonances at $\delta \sim 1.4$ ppm. As observed in Fig. 3(a) and (b), the hCH HETCOR data establishes an absence of

Table 1. Assignments and integrated intensities of the ^1H MAS NMR data acquired using a MAS frequency of 110 kHz (see Figure 2), presented with the ^1H T_1 data measured using saturation-recovery technique, and the T_2 data estimated from the FWHM of the assigned ^1H resonances.

Label	Assignment	^1H Chemical Shift δ (ppm)	Number of Protons	Integrated Intensity ($\pm 2\%$)	Theoretical Intensity (%)	^1H T_1 (s)	FWHM (Hz)/ ^1H T_2 (ms) ^b
1	PEA ⁺ aromatic	7.7	4	11.9	13.3	2.5 \pm 0.3	424 \pm 10/ \sim 0.7

2	PEA ⁺ aromatic	7.4	6	20.6	20	2.6±0.3	829±10/~0.4
3	PEA ⁺ NH ₃ ⁺	6.6	6	20.2	20	2.4±0.3	428±10/~0.7
4	MA ⁺ NH ₃ ⁺	6.3	3	11.2	10	2.8±0.3	352±10/~0.9
5,5'	PEA ⁺ α-CH ₂	4.2, 3.6	4	8.5, 4.4	8.4, 4.9 ^a	2.6±0.4	556±10/~0.6
6,6'	PEA ⁺ β-CH ₂	3.6, 3.1	4	4.7, 7.6	4.9, 8.4 ^a	2.6±0.4	572±10/~0.6
7	MA ⁺ CH ₃	3.1	3	10.9	10	3.1±0.4	329±10/~1.0
8	H ₂ O	1.4	-	-	-	-	-

^a) Estimates from the integrated intensities; ^b) Estimates from the FWHM of each resonance using the equation $\text{FWHM} = 1/(\pi T_2)$.

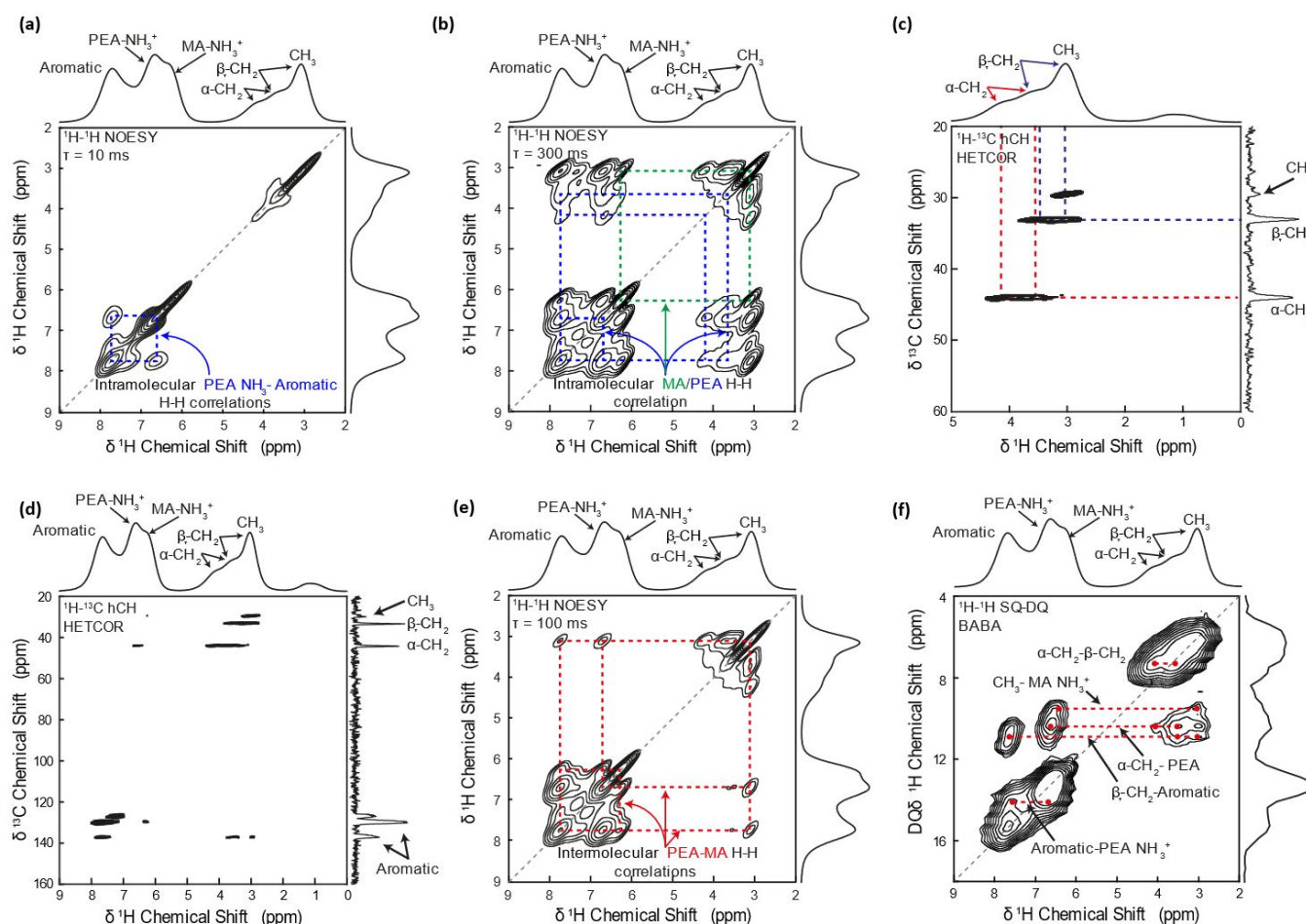


Fig. 3 Solid state 2D MAS NMR studies undertaken ($\nu_0 = 800.16$ MHz, $\nu_r = 110$ kHz) including, (a) the 2D heteronuclear ^1H - ^{13}C hCH HETCOR data, (b) an expansion of the aliphatic region of the 2D hCH HETCOR data highlighting the positional disorder in the ethylammonium substituent of the PEA⁺ cation, (c) the 2D homonuclear ^1H - ^1H DQ/SQ BABA data highlighting through-bond associations, and (d) - (f) the 2D homonuclear ^1H - ^1H NOESY data acquired with mixing times of 10, 100 and 300 ms, respectively, disclosing the through-space associations.

connectivity to any aliphatic or aromatic carbon species. Furthermore, the highly shielded (upfield) shift suggests that these H₂O position(s) that are distant from the PEA⁺ or MA⁺ amine cations, thus avoiding H-bonding arrangements that would introduce a deshielded (downfield) ^1H chemical shift. Previous studies have demonstrated that 2D perovskites exhibit a propensity for H₂O absorption.^{1,8} While the highly shielded ^1H shift shown in Fig. S2(a) and S3(a) suggests that these H₂O molecules reside in the inter-planar spacing between the

aromatic rings of the PEA⁺ cations, other positions such as those near the $[\text{PbI}_7]^{3-}$ framework or within the cubooctahedral cage accommodating the MA⁺ cation may also be possible.

The positional disorder exhibited by the PEA⁺ cation emanates from different structural conformers associated with the positioning of the ethylamine side-chain, as shown by the 1D ^1H MAS NMR and 2D ^1H - ^{13}C hCH HETCOR data (see Fig. 2(a), and 3(a) and (b), respectively). These conformers differ markedly in

the proximity of the amine functionality with respect to the aromatic ring. PEA⁺ conformer 1 positions the amine functionality at a maximum distance away from the aromatic ring, while PEA⁺ conformer 2 suggests that the aliphatic side-chain and amine moiety wrap back towards the aromatic ring introducing much closer contact. Direct evidence for this conformational isomerism is provided by both the 2D homonuclear ¹H-¹H double quantum/single quantum (DQ/SQ) BAcK-to-BAcK (BABA) and 2D homonuclear ¹H-¹H NOESY experiments.^{43,44}

The former experiment provides short-range information that relies on the selection of DQ dipolar coherence. As depicted in Fig. 3(c), the 2D ¹H-¹H BABA data show correlations (highlighted in red) that emphasize the expected short range correlations that are fundamental to the structure of the PEA⁺ and MA⁺ cations; however, this data also reveals evidence for the occurrence of conformer 2 with a short range aromatic-NH₃⁺(PEA) correlation between the ¹H shifts at δ 7.6 ppm and δ 6.6 ppm.

In contrast, the 2D homonuclear ¹H-¹H NOESY data of Fig. 3(d)-(f) are sensitive to longer range dipolar through-space interactions between nuclear spins. The spatial sensitivity limits of the NOESY technique are $\sim 2 - 3$ times that of the BABA experiment with the NOESY experiment able to detect correlated dipolar interactions out to ~ 6 Å,^{45,46} thus making it a powerful complement to the BABA approach. Due to its elongated arrangement of the pendant ethylamine sidechain into the free volume towards the 2D perovskite surface bisecting the PbI₆ octahedra, the PEA-NH₃⁺ moiety of conformer 1 is unlikely to experience a significant homonuclear ¹H-¹H dipolar interaction with the phenyl group anchoring the molecule. Although not measured in the 2D ¹H-¹H NOESY data utilizing a short 10 ms mixing time (see Fig. 3(f)), experiments employing longer mixing times of 100 and 300 ms detect weak-moderately strong intermolecular off-diagonal correlations between the PEA-NH₃⁺ moiety (δ 6.6 ppm) of conformer 1 and the CH₃ group of MA⁺ (δ 3.1 ppm) in the next-nearest-neighbor cuboctahedral cavity (see the data in Fig. 3(e) and (f), respectively). Such a spatial relationship must be confined to be within the ~ 6 Å detection limit of this experiment. This scenario differs markedly from the evidence supporting the local structure of PEA conformer 2 where intense intramolecular off-diagonal correlations are exhibited in the 2D ¹H-¹H NOESY data of 3s 2(d)-(f) relating the chemical shifts of the aromatic protons (δ 7.6 ppm) with the PEA-NH₃⁺ moiety (δ 6.6 ppm) for mixing times as short as 10 ms. These observations emphasize the strong homonuclear ¹H-¹H dipolar interaction between these proton species, and corroborates the 2D ¹H-¹H BABA data above (see Fig. 3(c)). These findings contrast with those from low field (2.35 T)/broadline ¹H T_1 relaxation measurements and mid-field (9.4 T) ¹³C T_1 relaxation measurements on the more ordered (PEA)₂[PbI₄] system which highlight no detectable disorder in the NH₃⁺ position of the PEA⁺ cation.^{47,48}

The structural disorder based solely around discrete PEA⁺ conformers outlined above is only a simplistic representation of the total disorder (and disruption to the H-bonding network) characterizing the PEA⁺ cations in the organic sublattice. As illustrated in Fig. S3(a) and (b), realistic descriptions must accommodate more complex arrangements such as in-plane and out-of-plane conformers, head-head and head-tail stacking, and orientational stacking faults that are underpinned by the basic PEA⁺ cation conformers proposed above. The breadth of this phase transition suggests that it is comprised of thermal re-ordering processes within a highly disordered network comprised of distributions of these structural realizations within the PEA⁺ cation network. This is supported by the ¹H T_2 values provided in Table 1 which are 3 - 4 orders of magnitude shorter than the corresponding T_1 values, thus suggesting that the correlation times of reorientation are slow. As shown in Fig. S4(b) for a dominant dipolar relaxation mechanism, the divergent T_1 and T_2 values are characteristic of correlation times that are on the slow motion side of the extreme narrowing limit in a regime normally associated with polymers and macromolecules. The disordered PEA⁺ cations in the 2D channels form a highly occluded network lacking cooperative modes of fast motion. Furthermore, the broad 1D ¹H MAS NMR resonances of Fig. 2(a) and 2D ¹H-¹H MAS NMR contours observed within Fig. 3(c)-(d) are influenced by widespread chemical shift dispersion. It is important to note that, although these measurements are performed under ultra-fast MAS conditions ($\nu_r = 110$ kHz), this dispersion is unable to be averaged (and resonances further narrowed) by these ultra-fast MAS frequencies. The extent of the disorder represented in the ¹H MAS NMR data, coupled with the very broad second-order phase transition characteristics identified in the DSC data, are consistent with the XRD results which are limited to the location of the inorganic framework positions only.

Optical Properties

An exfoliated (PEA)₂(MA)[Pb₂I₇] sample exhibits strong excitonic photoluminescence and absorbance at room temperature due to intrinsic crystallographic quantum confinement (see Fig. 4 (a)).^{49,50} The optical images are presented as supplementary information in Fig. S5. The photoluminescence (PL) data in Fig. S6(a)-(c) were simulated using asymmetric pseudo-Voigt peaks which accounted for both homogeneous and inhomogeneous broadening,⁵¹ while Fig. S6(d)-(f) shows that the evolution of the excitonic absorption edge was monitored by applying a linear fit to the lower energy slope of the optical absorbance (OA) spectra.

As observed in Fig. 4 and S7, the PL and the OA exhibit no abrupt intensity or frequency changes during cooling above 200 K apart from the gradual narrowing of the full-width-at-half-maximum (FWHM) which is ascribed to phonon population depletion. The excitonic absorption energy is almost unchanged during cooling from room temperature before a distinct blueshift of ~ 5 meV below 200 K, and it shows continuous redshift below 150 K (see Fig. 4(b) and S7(a)). An earlier study of (PEA)₂(MA)[Pb₂I₇] reported a small continuous red shift in absorption between 10

- 293 K with absorption peak asymmetry providing inconclusive evidence of a phase transition.^{37,52} The integrated PL intensity exhibited in Fig. 4(d) generally increases during cooling with a discontinuity at ~200 K appearing concomitantly with the excitonic anomaly. A similar evolution of the optical properties was observed under decreasing and increasing temperature regimes (see Fig. 4 and S7, respectively). The combined data provided by the differential scanning calorimetry (DSC) results of Fig. 4c and the optical spectroscopy provides corroborating evidence of a very broad and diffuse second-order phase transition phenomenon extending over the 150 - 200 K range.

Photoluminescence decreases with heating due to thermal quenching,^{18,53} whereby the integrated PL intensity conforms to:^{29,54}

$$I = \frac{I_0}{1 + \alpha e^{\left(\frac{-E_a}{kT}\right)}} \quad (1)$$

where I_0 is PL intensity at 0 K, E_a is the activation energy and α is a ratio of radiative and non-radiative lifetimes at 0 K. The fitting of the logarithmic integrated PL intensity vs inverse temperature is shown in Fig. 4(d). The activation energy of 250(40) meV measured from the room temperature phase was much larger than the value of 125(10) meV elucidated from the low temperature polymorph. This latter energy value is significantly smaller than reported exciton binding energy value of 170 meV.⁵² These results, together with the significant reduction in PL intensity at 200 K, suggests that the transformation into the low temperature phase introduces non-radiative pathways through the formation of longer-lived defect structures via reduced I^- and Pb^{2+} migration throughout the framework.^{29,43} Both Pb^{2+} and (in particular) I^- defects can be associated with stacking faults influencing some elements of the PEA^+ cation disorder in the 2D channels, and also introduces distributions within the shape, size and tilting of the cuboctahedral cavity thus affecting the MA^+ dynamics. These

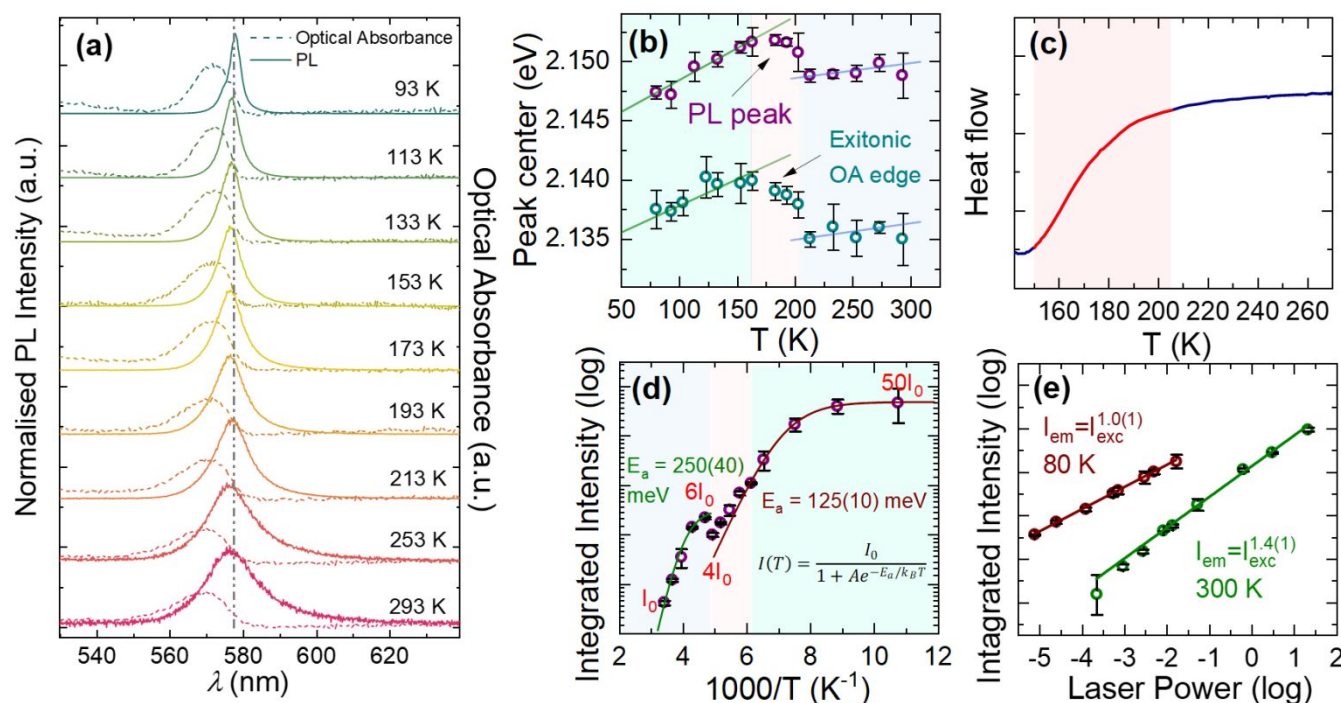


Fig. 4 Photophysical and thermal data from the $(PEA)_2(MA)[Pb_2I_7]$ system including, (a) photoluminescence (PL, 457 nm excitation) and optical absorbance (OA) of $(PEA)_2(MA)[Pb_2I_7]$ measurements acquired over a 93 - 293 K temperature range showing normalized PL and OA evolution under decreasing temperature, (b) plot of the PL peak maximum (purple) and the excitonic absorption edge (cyan) versus temperature, (c) differential scanning calorimetry (DSC) curves showing the gradual phase change in the temperature range from ~200 to 150 K (the shape of the curve suggests the second order phase transition), (d) plot of integrated PL intensity (logarithmic scale) versus $1/T$ as fitted by Equation 1, and (e) plot of intensity integrated PL intensity (logarithmic scale) versus laser excitation power (logarithmic scale) measured at room temperature (pink) and at 80K (green) with the slope of the linear fits reflecting the power coefficient of the dependence and the recombination mechanism.

assertions corroborate the findings of the 1H MAS NMR study and shape the structure/function relationship of the material. At lower extremes of the phase transition (~150 K), reduced ionic migration at throughout the inorganic $[Pb_2I_7]^{3-}$ framework is directly associated with attenuated rotational modes and slower motional dynamics throughout the disordered organic sublattice.

PL intensity is proportional to excitation intensity with a power law coefficient k , $I(PL) \sim P^k$, where the coefficient $k = 1$ describes free exciton recombination, $k = 1.5$ describes trapped exciton recombination, and $k = 2$ relates to bimolecular free carrier recombination.^{55,56} Therefore, defect-related recombination pathways can be examined using excitation intensity dependent experiments. Fig. 4(e) shows the log-log graphs of integrated PL intensity of $(\text{PEA})_2(\text{MA})[\text{Pb}_2\text{I}_7]$ with excitation power having slopes of 1.5 at room temperature, consistent with non-radiative defects, and 1 at low temperature, suggesting an absence of defects. However, it is noted that defects may not be activated at 80 K

Methylammonium Dynamics

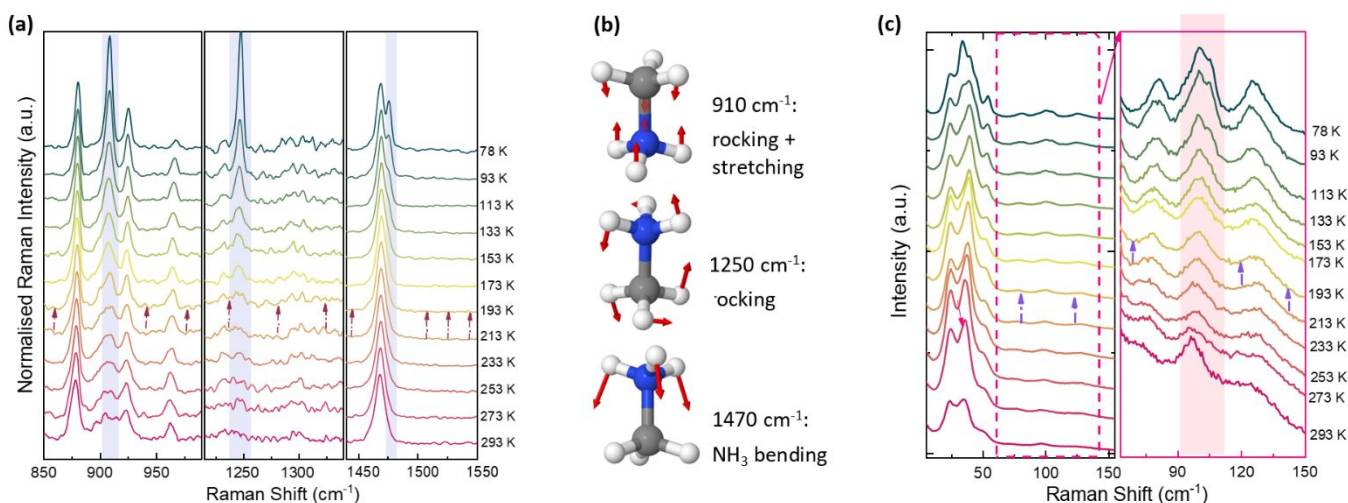


Fig. 5 Raman data from the $(\text{PEA})_2(\text{MA})[\text{Pb}_2\text{I}_7]$ system showing, (a) the high wavenumber spectra measured over the temperature range of 78 - 293 K, and (b) a schematic depiction of the assignments of the MA^+ vibrational modes. In (a) the MA^+ modes are highlighted and the red points indicate the onset of the broad phase transition phenomenon. (c) Raman data from the $(\text{PEA})_2(\text{MA})[\text{Pb}_2\text{I}_7]$ system showing ultra-low wavenumber spectra measured over the temperature range of 78 - 293 K.

vibrations. The relative intensity of the 910 cm^{-1} (ρ MA^+) band increases continuously below ~ 200 K, while the intensity of the bands at 1247 cm^{-1} (ρ MA^+) and 1478 cm^{-1} (δ NH_3^+) increase below ~ 200 K (see Fig. 5). It is important to note that the C-N bond stretching frequency and intensity do not undergo any changes with temperature, confirming that only one end (rather than both ends) of the MA^+ cation is involved in the phase transition. Thus, spectral changes involving the NH_3^+ bending or rocking vibrations demonstrate that the phase transition is strongly associated with the NH_3^+ moiety and its participation within the hydrogen bonding network.

As shown in Fig. 5(c), further evidence of a low temperature dimorph of $(\text{PEA})_2(\text{MA})[\text{Pb}_2\text{I}_7]$ is observed by low wavenumber Raman spectroscopy. It is notable that distinct bands below <150 cm^{-1} persist even at room temperature as the PEA^+ cations are relatively static and do not participate in large amplitude vibrations. This observation is consistent with the ^1H MAS NMR study that is characterized by broad resonance linewidths and short T_2 s from slower motional correlation times and occluded structural disorder. Furthermore, this feature is in sharp

contrast to that observed in 3D perovskites which only exhibit broad Raman bands due to dynamic MA⁺ and FA⁺ disorder,^{10,31,57} emphasizing that the presence of the PEA⁺ cations induce a more rigid inorganic sublattice with distinct low wavenumber Raman bands. The bands below ~ 30 cm⁻¹ are attributed to PbI₆ tilting modes, those below 80 cm⁻¹ are assigned to I-Pb-I bending modes, the peaks between 80 cm⁻¹ and 150 cm⁻¹ are assigned to Pb-I stretches, while those bands <50 cm⁻¹ cannot be assigned unique Raman modes. Nevertheless, temperature dependent features are evident in Fig. 5(c). For instance, the feature at ~ 30 cm⁻¹ is distinct only after cooling, while the mode at 100 cm⁻¹, assigned to Pb-I stretching in the PbI₆ octahedron, develops a splitting. This phenomenon is caused by octahedral distortion resulting in the improved peak resolution due to the formation of a more ordered and rigid structure; this assertion is supported by increased hydrogen bonding at low temperatures.⁵⁸ These temperature dependent features in the variable temperature Raman data of Fig. 5(c) infer a discontinuous evolution of crystal structure at around 200 K that is consistent with the other evidence of the ill-defined phase transition.

The ¹H MAS NMR data presented in Table 1 corroborates the Raman findings reported above. As shown in Fig. S9, the octahedral tilting induces a reduction in the I-Pb-I angle (labelled α) to $\sim 155^\circ$; this represents a substantial distortion from 179° measured from the MAPbI₃ structure at room temperature.⁵⁹ This octahedral tilt distorts the bond lengths, bond angles and shape of the cuboctahedral cavities accommodating the MA⁺ cations. The volume of the cavity, containing MA⁺ cations, decreases from $\sim 80 \text{ \AA}^3$ in tetragonal phase of the 3D MAPbI₃ to $\sim 50 \text{ \AA}^3$ in (PEA)₂(MA)[Pb₂I₇] (Fig. S10). In this case the degrees of freedom available for the MA⁺ cation motion become restricted, thus resulting in altered MA⁺ dynamics in comparison to MAPbI₃. The MA⁺ cation dynamics in MAPbI₃ at room temperature has been shown to undergo ultra-fast reorientation using quasi elastic neutron scattering, GHz spectroscopy, ¹⁴N NMR and electron diffraction, with the resulting rotational correlation times (τ_{rot}) residing in the picosecond range.^{60–62} The reorientation dynamics of MA⁺ in MAPbI₃ have also been investigated using ¹H T_1 relaxation experiments,^{59,61,63,64} with Kubicki *et al.* reporting the ¹H T_1 of the CH₃ and NH₃⁺ moieties to be ~ 16 s when measured at high field (21.1 T, 900 MHz).⁶⁴ In the present study, similar high field ¹H T_1 measurements (18.8 T, 800 MHz) were undertaken on (PEA)₂(MA)[Pb₂I₇], with the summarized results of Table 1 and Fig. 6 describing significantly shorter ¹H T_1 s characterizing the MA⁺ and PEA⁺ cation dynamics within this system. As represented in Fig. 6, the saturation-recovery T_1 data has been fitted with single exponential functions, with all measured ¹H T_1 values falling within a narrow range of $\sim 2.4 - 3.1$ s.

The different T_1 ranges characterizing the MAPbI₃ and (PEA)₂(MA)[Pb₂I₇] systems, and the diverse motional regimes that they represent, are highlighted in Fig. S4(b). While the MA⁺ cation dynamics of the 3D ($n = \infty$) MAPbI₃ perovskite (characterised by longer T_1 s and no octahedral tilting) places it

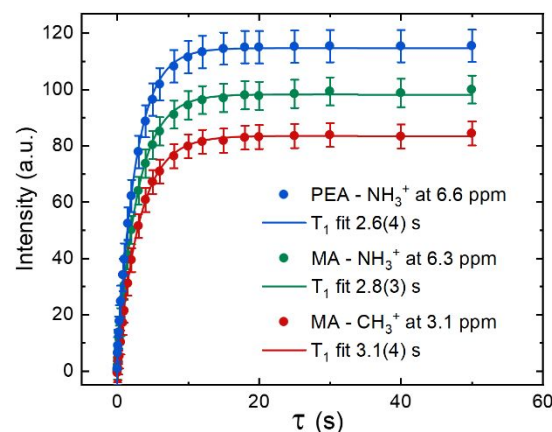


Fig. 6 ¹H T_1 data from the MA⁺ CH₃ (red) and NH₃⁺ (green) proton species, and the PEA⁺ NH₃⁺ (blue) proton species, measured with the saturation-recovery technique.

in fast motional regime on the right of the extreme narrowing limit, the MA⁺ and PEA⁺ cation dynamics of the 2D ($n = 2$) (PEA)₂(MA)[Pb₂I₇] perovskite (characterised by shorter T_1 s, divergent T_1 and T_2 values and significant octahedral tilting) reside on the opposite side in the slow motional regime. The octahedral tilting underpinning the (PEA)₂(MA)[Pb₂I₇] framework is a key feature of the overall system. In addition to the smaller distorted cuboctahedra environments inducing restricted MA⁺ cation dynamics, I⁻ and Pb²⁺ defects (and associated ion migration) introduce additional framework disorder including distributions within the octahedral tilting, dislocations and misalignment within the 2D channels which directly translate into the disordered PEA⁺ environments reported above. These effects have been proposed in previous structural, computational and photophysical studies on similar 2D hybrid perovskite systems.^{65,66}

The optical and Raman spectroscopic results consistently demonstrate a broad phase change commencing at 200 K which is attributed to MA⁺ dynamics and its hydrogen bonding state. In particular, the Raman study provides unambiguous evidence that part of the evolution of the organic sublattice with temperature involves the vibrations of the NH₃⁺ constituent of the MA⁺ cation. These spectral changes are manifested from MA⁺ ordering through hydrogen bonding that promotes harmonic vibrations and a more rigid structure, thus yielding more intense and narrower bands as demonstrated from previous studies for 3D perovskites MAPbX₃ ($X = \text{Br}, \text{I}$).^{10,31,43,67} vertheless, the ¹H MAS NMR study indicates that the timescale of MA⁺ motion in (PEA)₂(MA)[Pb₂I₇] is much slower than that in MAPbI₃ by approximately four orders of magnitude; as outlined above, this is governed by distortion of the cuboctahedral cavities. In contrast, the PEA⁺ component of the organic sublattice also contributes to the broad phase change behavior through different thermally driven mechanisms of reorientation. It represents a connected organic network of highly occluded and disordered cations that also participates in

slow molecular reorientation and is also underpinned by the ^1H MAS NMR data. The contrasting influences dominating the different parts of the organic sublattice suggest that the observed broad phase transition of Fig. 4(b) is highly inhomogeneous, and the overall thermal response probably represents a superposition of discrete thermal rearrangement processes pertaining to the MA^+ and PEA^+ cations.

Previous single crystal X-ray diffraction measurements on the $(\text{PEA})_2(\text{MA})[\text{Pb}_2\text{I}_7]$ system³⁶ and those undertaken within this study, have been unable to elucidate a structural determination of the complete system. While longer-range periodic elements defining the inorganic $[\text{Pb}_2\text{I}_7]^{3+}$ framework can be determined, the short-range structural detail yielding the exact coordinates of the MA^+ or PEA^+ cations is hindered by the structural disorder within the organic sublattice, as demonstrated by the solid state NMR technique. This precludes a measure of the hydrogen-bonding lengths influencing the MA^+ cations and further corroboration of the effects observed in the Raman data. A full DFT computational analysis of the statistical distributions of structural realisations generated to simulate the disorder within the organic sublattice is being undertaken to support the spectroscopic and thermal response observations reported for the first time.

Conclusions

In this work, the significant structural disorder characterizing the MA^+ and PEA^+ cations constituting the organic sublattice within the 2D ($n = 2$) $(\text{PEA})_2(\text{MA})[\text{Pb}_2\text{I}_7]$ system as reported by the ^1H and ^{13}C MAS NMR technique has been presented with photophysical and Raman spectroscopic studies characterizing this material. The structural disorder described in this work represents the first rationalization of disorder for 2D hybrid perovskites, and it corroborates the partial structural solution (inorganic framework only) obtained by single crystal X-ray diffraction and the very broad phase transition as exhibited by the DSC data. The phase transition observed to occur over a 200 - 150 K temperature range is probably an inhomogeneous process involving the rearrangement of both the MA^+ and PEA^+ cations in discrete thermally driven processes. While the ^1H MAS NMR data demonstrates that the MA^+ dynamics in 2D $(\text{PEA})_2(\text{MA})[\text{Pb}_2\text{I}_7]$ is slow in comparison to its 3D MAPbI_3 counterpart (by approximately four orders of magnitude), the Raman study shows that the MA^+ hydrogen bonding network is strengthened over this temperature range. The importance of MA^+ dynamics over this temperature range on the changing photophysical and optical properties was also emphasized for this 2D perovskite system. In addition, the ^1H MAS NMR data determines that the PEA^+ cations are also in a slow motional regime, and the structural disorder comprised of conformational isomers and stacking and orientational dislocations produce a highly occluded network down the 2D channels that also structurally readjusts over this temperature range. Furthermore, the ability for these 2D channel structures to absorb water was observed, thus potentially augmenting the disorder phenomenon throughout the PEA^+ cation network.

Author Contributions

We strongly encourage authors to include author contributions and recommend using CRediT for standardised contribution descriptions. Please refer to our general author guidelines for more information about authorship.

Conflicts of interest

There are no conflicts to declare.

Acknowledgements

The authors gratefully acknowledge Ministry of Education of Singapore for the funding of this research through the following grants, AcRF Tier 1 (Reference No: RG195/17 and RG156/19); AcRF Tier 3 (MOE2016-T3-1-006 (S)). JVH and ZXS also acknowledges the Centre of High Field NMR Spectroscopy and Imaging, and the Facility for Analysis, Characterization, Testing and Simulation (FACTS) at NTU, Singapore, for access to their solid state NMR, electron microscopy and X-ray diffraction facilities.

Notes and references

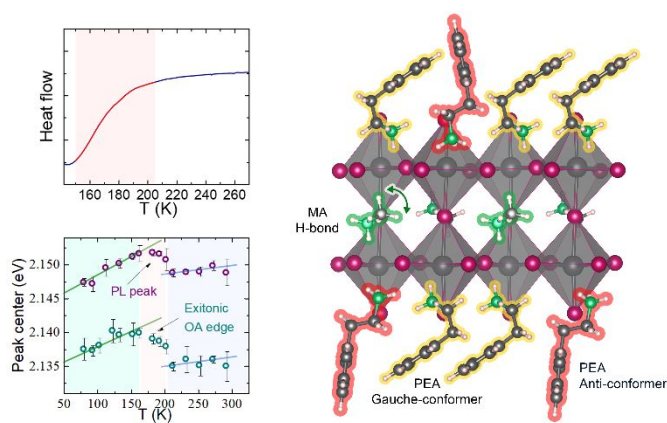
- Q. Chen, N. De Marco, Y. Yang, T. Bin Song, C. C. Chen, H. Zhao, Z. Hong, H. Zhou and Y. Yang, *Nano Today*, 2015, 10, 355–396.
- M. M. Lee, J. Teuscher, T. Miyasaka, T. N. Murakami and H. J. Snaith, *Science* 2012, 338, 643–647.
- K. P. Marshall, M. Walker, R. I. Walton and R. A. Hatton, *Nat. Energy*, 2016, 1, 16178.
- A. Sadhanala, S. Ahmad, B. Zhao, N. Giesbrecht, P. M. Pearce, F. Deschler, R. L. Z. Hoyer, K. C. Gödel, T. Bein, P. Docampo, S. E. Dutton, M. F. L. De Volder and R. H. Friend, *Nano Lett.*, 2015, 15, 6095–6101.
- M. L. Lai, T. Y. S. S. Tay, A. Sadhanala, S. E. Dutton, G. Li, R. H. Friend and Z. K. Tan, *J. Phys. Chem. Lett.*, 2016, 7, 2653–2658.
- M. D. Birowosuto, D. Cortecchia, W. Drozdowski, K. Brylew, W. Lachmanski, A. Bruno and C. Soci, *Sci. Rep.*, 2016, 6, 37254.
- S. Yakunin, M. Sytnyk, D. Kriegner, S. Shrestha, M. Richter, G. J. Matt, H. Azimi, C. J. Brabec, J. Stangl, M. V. Kovalenko and W. Heiss, *Nat. Photonics*, 2015, 9, 444–449.
- L. Pedesseau, D. Saporì, B. Traore, R. Robles, H. H. Fang, M. A. Loi, H. Tsai, W. Nie, J. C. Blancon, A. Neukirch, S. Tretiak, A. D. Mohite, C. Katan, J. Even and M. Kepenekian, *ACS Nano*, 2016, 10, 9776–9786.
- G. Xing, N. Mathews, S. S. Lim, N. Yantara, X. Liu, D. Sabba, M. Grätzel, S. Mhaisalkar and T. C. Sum, *Nat. Mater.*, 2014, 13, 476–480.
- R. G. Niemann, A. G. Kontos, D. Palles, E. I. Kamitsos, A. Kaltzoglou, F. Brivio, P. Falaras and P. J. Cameron, *J. Phys. Chem. C*, 2016, 120, 2509–2519.
- J. Li, H. Wang, X. Y. Chin, H. A. Dewi, K. Vergeer, T. W. Goh, J. W. M. Lim, J. H. Lew, K. P. Loh, C. Soci, T. C. Sum, H. J. Bolink, N. Mathews, S. Mhaisalkar and A. Bruno, *Joule*, 2020, 4, 1035–1053.
- F. Sahli, J. Werner, B. A. Kamino, M. Bräuninger, R. Monnard, B. Paviet-Salomon, L. Barraud, L. Ding, J. J. Diaz Leon, D. Sacchetto, G. Cattaneo, M. Despeisse, M. Boccard, S. Nicolay, Q. Jeangros, B. Niesen and C. Ballif, *Nat. Mater.*, 2018, 17, 820–826.

- 13 M. A. Green, E. D. Dunlop, J. Hohl-Ebinger, M. Yoshita, N. Kopidakis and X. Hao, *Prog. Photovoltaics Res. Appl.*, 2020, 28, 629–638.
- 14 C. C. Stoumpos, C. M. M. Soe, H. Tsai, W. Nie, J. C. Blancon, D. H. Cao, F. Liu, B. Traoré, C. Katan, J. Even, A. D. Mohite and M. G. Kanatzidis, *Chem*, 2017, 2, 427–440.
- 15 X. Gan, O. Wang, K. Liu, X. Du, L. Guo and H. Liu, *Sol. Energy Mater. Sol. Cells*, 2017, 162, 93–102.
- 16 Y. Wei, P. Audebert, L. Galmiche, J. S. Lauret and E. Deleporte, *Materials (Basel)*, 2014, 7, 4789–4802.
- 17 N. Wang, L. Cheng, R. Ge, S. Zhang, Y. Miao, W. Zou, C. Yi, Y. Sun, Y. Cao, R. Yang, Y. Wei, Q. Guo, Y. Ke, M. Yu, Y. Jin, Y. Liu, Q. Ding, D. Di, L. Yang, G. Xing, H. Tian, C. Jin, F. Gao, R. H. Friend, J. Wang and W. Huang, *Nat. Photonics*, 2016, 10, 699–704.
- 18 M. Yuan, L. N. Quan, R. Comin, G. Walters, R. Sabatini, O. Voznyy, S. Hoogland, Y. Zhao, E. M. Beauregard, P. Kanjanaboos, Z. Lu, D. H. Kim and E. H. Sargent, *Nat. Nanotechnol.*, 2016, 11, 872–877.
- 19 Z. Wang, Q. Lin, F. P. Chmiel, N. Sakai, L. M. Herz and H. J. Snaith, *Nat. Energy*, 2017, 2, 17135.
- 20 D. B. Mitzi, *J. Chem. Soc. Dalt. Trans.*, 2001, 1–12.
- 21 C. C. Stoumpos, D. H. Cao, D. J. Clark, J. Young, J. M. Rondinelli, J. I. Jang, J. T. Hupp and M. G. Kanatzidis, *Chem. Mater.*, 2016, 28, 2852–2867.
- 22 M. E. Kammaing, H. H. Fang, M. R. Filip, F. Giustino, J. Baas, G. R. Blake, M. A. Loi and T. T. M. M. Palstra, *Chem. Mater.*, 2016, 28, 4554–4562.
- 23 Y. Takeoka, M. Fukasawa, T. Matsui, K. Kikuchi, M. Rikukawa and K. Sanui, *Chem. Commun.*, 2005, 378–380.
- 24 A. Vassilakopoulou, D. Papadatos, I. Zakouras and I. Koutselas, *J. Alloys Compd.*, 2017, 692, 589–598.
- 25 T. Umebayashi, K. Asai, T. Umebayashi, K. Asai, T. Kondo, T. Kondo and A. Nakao, *Phys. Rev. B - Condens. Matter Mater. Phys.*, 2003, 67, 155405.
- 26 D. Cortecchia, S. Neutzner, A. R. S. Kandada, E. Mosconi, D. Meggiolaro, F. De Angelis, C. Soci and A. Petrozza, *J. Am. Chem. Soc.*, 2017, 139, 39–42.
- 27 J. Yin, H. Li, D. Cortecchia, C. Soci and J. L. Brédas, *ACS Energy Lett.*, 2017, 2, 417–423.
- 28 S. T. Ha, C. Shen, J. Zhang and Q. Xiong, *Nat. Photonics*, 2016, 10, 115–121.
- 29 K. Gauthron, J. Lauret, L. Doyennette, G. Lanty, A. Al Choueiry, S. J. Zhang, A. Brehier, L. Largeau, O. Mauguin, J. Bloch and E. Deleporte, *Opt. Express*, 2010, 18, 5912.
- 30 F. Brivio, J. M. Frost, J. M. Skelton, A. J. Jackson, O. J. Weber, M. T. Weller, A. R. Goñi, A. M. A. A. Leguy, P. R. F. Barnes and A. Walsh, *Phys. Rev. B - Condens. Matter Mater. Phys.*, 2015, 92, 1–8.
- 31 T. Yin, Y. Fang, X. Fan, B. Zhang, J.-L. Kuo, T. J. White, G. M. Chow, J. Yan and Z. X. Shen, *Chem. Mater.*, 2017, 29, 5974–5981.
- 32 J. H. Lee, N. C. Bristowe, P. D. Bristowe and A. K. Cheetham, *Chem. Commun.*, 2015, 51, 6434–6437.
- 33 J. H. J. H. J. H. Lee, J. H. J. H. J. H. Lee, E. H. Kong and H. M. Jang, *Sci. Rep.*, 2016, 6, 1–12.
- 34 F. El-Mellouhi, A. Marzouk, E. T. Bentría, S. N. Rashkeev, S. Kais and F. H. Alharbi, *ChemSusChem*, 2016, 9, 2648–2655.
- 35 J. Yin, P. Maity, L. Xu, A. M. El-Zohry, H. Li, O. M. Bakr, J.-L. L. Brédas and O. F. Mohammed, *Chem. Mater.*, 2018, 3, acs.chemmater.8b03436.
- 36 J. Calabrese, N. L. Jones, R. L. Harlow, N. Herron, D. L. Thorn and Y. Wang, *J. Am. Chem. Soc.*, 1991, 113, 2328–2330.
- 37 T. Kataoka, T. Kondo, R. Ito, S. Sasaki, K. Uchida and N. Miura, *Phys. B Phys. Condens. Matter*, 1994, 201, 423–426.
- 38 C. Quarti, G. Grancini, E. Mosconi, P. Bruno, J. M. Ball, M. M. Lee, H. J. Snaith, A. Petrozza and F. De Angelis, *J. Phys. Chem. Lett.*, 2014, 5, 279–284.
- 39 D. Massiot, F. Fayon, M. Capron, I. King, S. Le Calvé, B. Alonso, J. O. Durand, B. Bujoli, Z. Gan and G. Hoatson, *Magn. Reson. Chem.*, 2002, 40, 70–76.
- 40 J. P. Perdew, J. A. Chevary, S. H. Vosko, K. A. Jackson, M. R. Pederson, D. J. Singh and C. Fiolhais, *Phys. Rev. B*, 1992, 46, 6671–6687.
- 41 K. Lee, É. D. Murray, L. Kong, B. I. Lundqvist and D. C. Langreth, *Phys. Rev. B - Condens. Matter Mater. Phys.*, 2010, 82, 3–6.
- 42 W. Peng, J. Yin, K. T. Ho, O. Ouellette, M. De Bastiani, B. Murali, O. El Tall, C. Shen, X. Miao, J. Pan, E. Alarousu, J. H. He, B. S. Ooi, O. F. Mohammed, E. Sargent and O. M. Bakr, *Nano Lett.*, 2017, 17, 4759–4767.
- 43 P. Vashishtha, S. A. Veldhuis, S. S. H. Dintakurti, N. L. Kelly, B. E. Griffith, A. A. M. Brown, M. S. Ansari, A. Bruno, N. Mathews, Y. Fang, T. White, S. G. Mhaisalkar and J. V. Hanna, *J. Mater. Chem. C*, 2020, 8, 11805–11821.
- 44 C. J. Dahlman, R. M. Kennard, P. Paluch, N. R. Venkatesan, M. L. Chabinyk and G. N. Manjunatha Reddy, *Chem. Mater.*, 2021, 33, 642–656.
- 45 D. Neuhaus, *Encycl. Magn. Reson.*, DOI:10.1002/9780470034590.emrstm0350.
- 46 J. De Roo, M. Ibáñez, P. Geiregat, G. Nedelcu, W. Walravens, J. Maes, J. C. Martins, I. Van Driessche, M. V. Kovalenko and Z. Hens, *ACS Nano*, 2016, 10, 2071–2081.
- 47 T. Ueda, M. Omo, K. Shimizu, H. Ohki and T. Okuda, *Zeitschrift für Naturforsch. A*, 1997, 52, 502–508.
- 48 T. Ueda, K. Shimizu, H. Ohki and T. Okuda, *Zeitschrift für Naturforsch. A*, 1998, 53, 7983–988.
- 49 D. Cortecchia, J. Yin, A. Bruno, S.-Z. A. Z. A. Lo, G. G. Gurzadyan, S. Mhaisalkar, J.-L. L. Brédas and C. Soci, *J. Mater. Chem. C*, 2017, 5, 1–34.
- 50 T. Ishihara, in *Optical Properties of Low-Dimensional Materials*, eds. T. Ogawa and Y. Kanemitsu, World Scientific, Singapore, 1995, pp. 289–339.
- 51 H. Diab, G. Trippé-Allard, F. Lédée, K. Jemli, C. Vilar, G. Bouchez, V. L. R. Jacques, A. Tejada, J. Even, J. S. Lauret, E. Deleporte and D. Garrot, *J. Phys. Chem. Lett.*, 2016, 7, 5093–5100.
- 52 X. Hong, T. Ishihara and A. V. Nurmikko, *Phys. Rev. B*, 1992, 45, 6961–6964.
- 53 K. Chondroudis and D. B. Mitzi, *Chem. Mater.*, 1999, 11, 3028–3030.
- 54 L. Gan, J. Li, Z. Fang, H. He and Z. Ye, *J. Phys. Chem. Lett.*, 2017, 8, 5177–5183.
- 55 T. Schmidt, K. Lischka and W. Zulehner, *Phys. Rev. B*, 1992, 45, 8989–8994.
- 56 S. Draguta, S. Thakur, Y. V. Morozov, Y. Wang, J. S. Manser, P. V. Kamat and M. Kuno, *J. Phys. Chem. Lett.*, 2016, 7, 715–721.
- 57 L. Wang, K. Wang and B. Zou, *J. Phys. Chem. Lett.*, 2016, 7, 2556–2562.
- 58 L. Mao, P. Guo, M. Kepenekian, I. Hadar, C. Katan, J. Even, R. D. Schaller, C. C. Stoumpos and M. G. Kanatzidis, *J. Am. Chem. Soc.*, 2018, 140, 13078–13088.
- 59 T. Baikie, N. S. Barrow, Y. Fang, P. J. Keenan, P. R. Slater, R. O. Piltz, M. Gutmann, G. Mhaisalkar, T. J. White, S. G. Mhaisalkar and T. J. White, *J. Mater. Chem. A*, 2015, 3, 9298–9307.
- 60 X. Wu, L. Z. Tan, X. Shen, T. Hu, K. Miyata, M. T. Trinh, R. Li, R. Coffee, S. Liu, D. A. Egger, I. Makasyuk, Q. Zheng, A. Fry, J. S. Robinson, M. D. Smith, B. Guzelturk, H. I. Karunadasa, X. Wang, X. Zhu, L. Kronik, A. M. Rappe and A. M. Lindenberg, *Sci. Adv.*,

ARTICLE

Journal Name

- 2017, 3, e1602388.
- 61 D. H. Fabini, T. A. Siaw, C. C. Stoumpos, G. Laurita, D. Olds, K. Page, J. G. Hu, M. G. Kanatzidis, S. Han and R. Seshadri, *J. Am. Chem. Soc.*, 2017, 139, 16875–16884.
- 62 A. M. A. A. Leguy, J. M. Frost, A. P. McMahon, V. G. Sakai, W. Kochelmann, C. Law, X. Li, F. Foglia, A. Walsh, B. C. O'Regan, J. Nelson, J. T. Cabral and P. R. F. F. Barnes, *Nat. Commun.*, , DOI:10.1038/ncomms8124.
- 63 G. M. Bernard, R. E. Wasylshen, C. I. Ratcliffe, V. Terskikh, Q. Wu, J. M. Buriak, T. Hauger, C. I. Ratcli, V. Terskikh, Q. Wu, J. M. Buriak, T. Hauger, C. I. Ratcliffe, V. Terskikh, Q. Wu, J. M. Buriak and T. Hauger, *J. Phys. Chem. A*, 2018, 122, 1560–1573.
- 64 D. J. Kubicki, D. Prochowicz, A. Pinon, G. Stevanato, A. Hofstetter, S. M. Zakeeruddin, M. Grätzel and L. Emsley, *J. Mater. Chem. A*, 2019, 7, 2326–2333.
- 65 K. Z. Du, Q. Tu, X. Zhang, Q. Han, J. Liu, S. Zauscher and D. B. Mitzi, *Inorg. Chem.*, 2017, 56, 9291–9302.
- 66 J. Hu, I. W. H. Oswald, S. J. Stuard, M. M. Nahid, N. Zhou, O. F. Williams, Z. Guo, L. Yan, H. Hu, Z. Chen, X. Xiao, Y. Lin, Z. Yang, J. Huang, A. M. Moran, H. Ade, J. R. Neilson and W. You, *Nat. Commun.*, 2019, 10, 1–11.
- 67 P. Vashishtha, S. Bishnoi, C. H. Angus Li, M. Jagadeeswararao, T. J. N. Hooper, N. Lohia, S. B. Shivarudraiah, M. S. Ansari, S. N. Sharma and J. E. Halpert, *ACS Appl. Electron. Mater.*, 2020, 2, 3470–3490.



Optical properties of the quasi-2D perovskite are related to the significant structural disorder involving both the MA⁺ and PEA⁺ cations

Supplementary Information

The Effect of Organic Cation Dynamics on the Optical Properties in $(\text{PEA})_2(\text{MA})[\text{Pb}_2\text{I}_7]$ Perovskite Dimorphs

Yulia Lekina,^{a,b} Sai S.H. Dintakurti,^{c,d} Benny Febriansyah,^e D.J. Bradley,^d Jiaxu Yan,^f Xiangyan Shi,^b Jason England,^e Tim White,^g John V. Hanna,^{*d,g} Ze Xiang Shen^{*a,b}

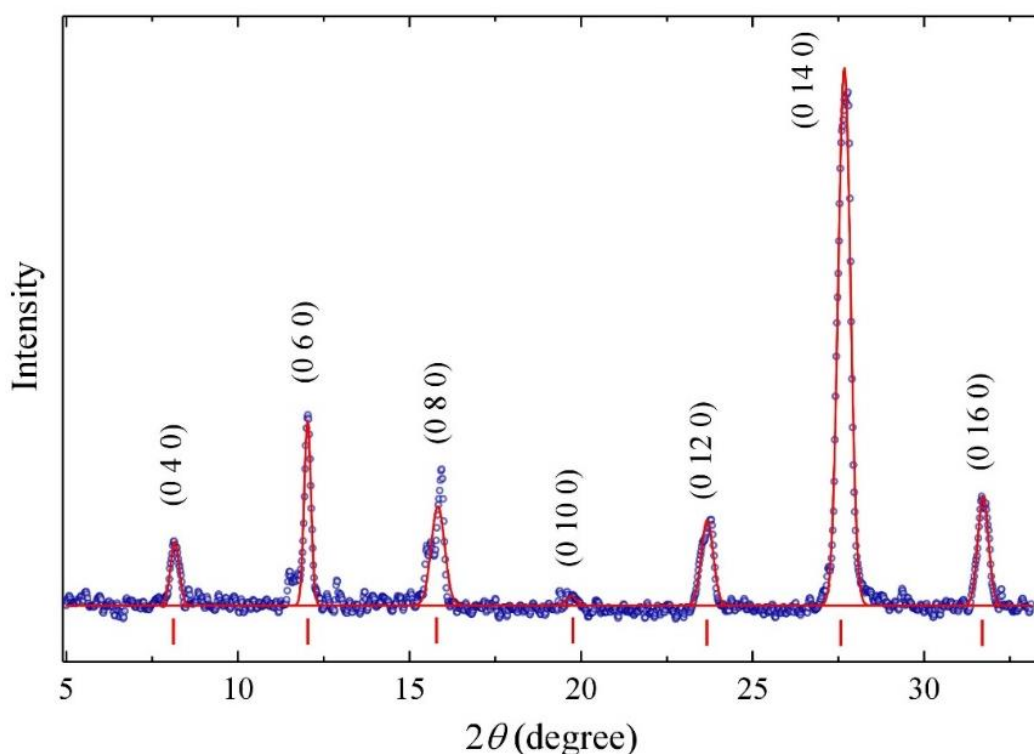


Figure S1. Powder XRD data of the horizontally oriented $\text{PEA}_2\text{MAPb}_2\text{I}_7$ platelets.

^a. Centre for Disruptive Photonic Technologies, Nanyang Technological University, 637371, Singapore.

^b. Division of Physics and Applied Physics, School of Physical and Mathematical Sciences, Nanyang Technological University, 637371, Singapore.

^c. Interdisciplinary Graduate School (IGS), Nanyang Technological University, 50 Nanyang Avenue, Singapore 639798, Singapore.

^d. Department of Physics, University of Warwick, Gibbet Hill Rd., Coventry CV4 7AL, UK

^e. Division of Chemistry and Biological Chemistry, School of Physical and Mathematical Sciences, Nanyang Technological University, 21 Nanyang Link, Singapore 637371, Singapore.

^f. Key Laboratory of Flexible Electronics (KLOFE) & Institute of Advanced Materials (IAM), Jiangsu National Synergistic Innovation Center for Advanced Materials (SICAM), Nanjing Tech University (Nanjing Tech), Nanjing 211816, China.

^g. School of Materials Science and Engineering, Nanyang Technological University, 50 Nanyang Avenue, Singapore 639798, Singapore

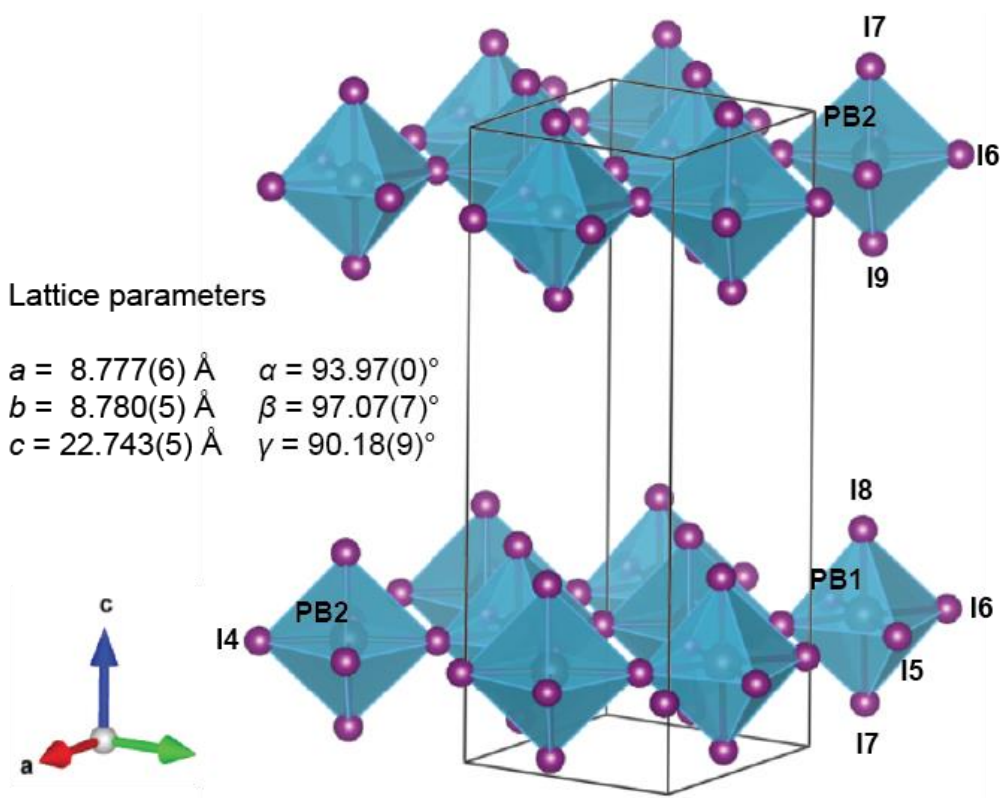


Figure S2. Structure $(\text{PEA})_2(\text{MA})[\text{Pb}_2\text{I}_7]$ obtained by single crystal X-Ray analysis and unit cell parameters. Only coordinates of inorganic atoms were determined.

Table S1. Refined positions and equivalent isotropic atomic displacement parameters obtained from best fit single crystal structural model.

Atom site	<i>x</i>	<i>y</i>	<i>z</i>	<i>U</i> _{eq} (Å ³)
PB1	0.29527(9)	0.77484(9)	0.14482(4)	0.0336(3)
PB2	0.79762(9)	0.27700(9)	0.14486(4)	0.0334(3)
I3	0.4915(2)	0.0771(2)	0.14074(9)	0.0526(5)
I4	-0.0076(2)	0.9730(2)	0.14142(9)	0.0549(5)
I5	0.0991(2)	0.4709(2)	0.14172(10)	0.0616(5)
I6	0.5973(2)	0.5774(2)	0.14138(9)	0.0551(5)
I7	0.2496(2)	0.7522(2)	0.00021(7)	0.0566(5)
I8	0.3507(3)	0.8041(3)	0.28379(9)	0.0626(5)
I9	0.8403(3)	0.2885(3)	0.28374(9)	0.0622(5)

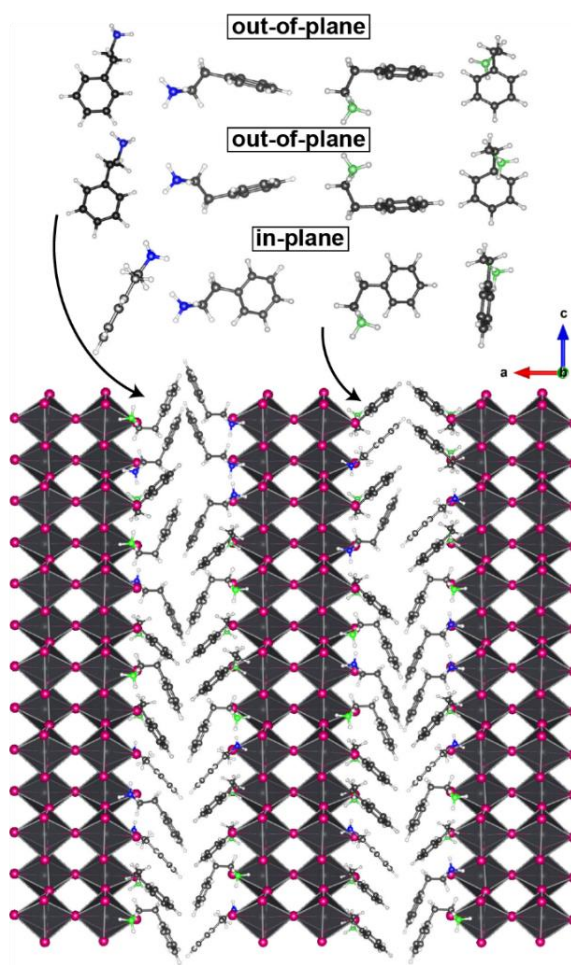
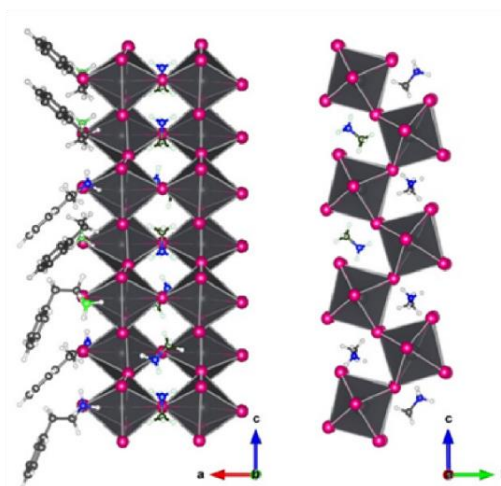
(a) *anti* conformers *gauche* conformers**(b)**

Figure S3. Schematic representations of the structural disorder in the organic sublattice as incurred (a) by the PEA⁺ cations in the 2D interlayer channels, and (b) by the MA⁺ cations in the octahedral cavities.

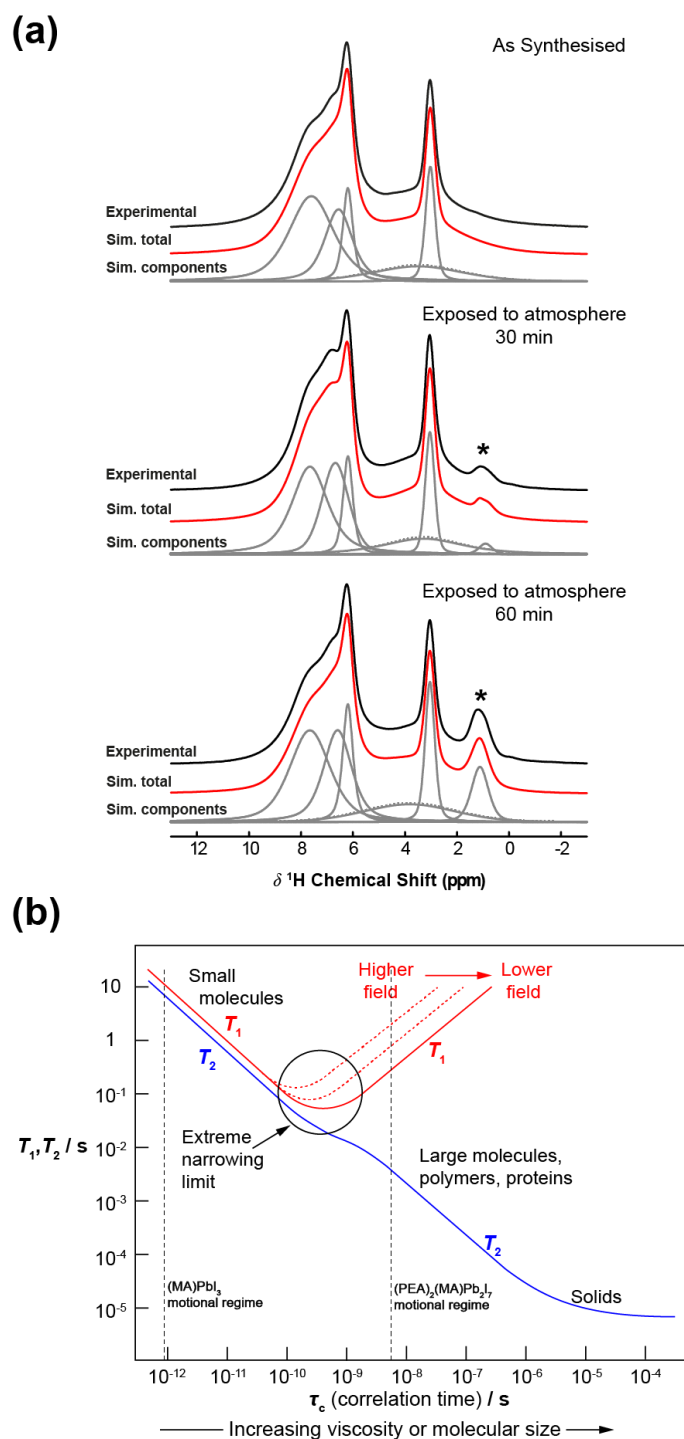


Figure S4. Additional ^1H MAS NMR characterisation of the $(\text{PEA})_2(\text{MA})[\text{Pb}_2\text{I}_7]$ system showing, (a) spectral evidence for H_2O absorption (H_2O resonance marked with an asterisk, $\nu_0 = 800.16$ MHz, $\nu_r = 35$ kHz) commensurate with increasing times of atmospheric exposure, and (b) mapping of the motional regime of the PEA^+ and MA^+ cations according the relationship between the ^1H T_1 and T_2 relaxation times.

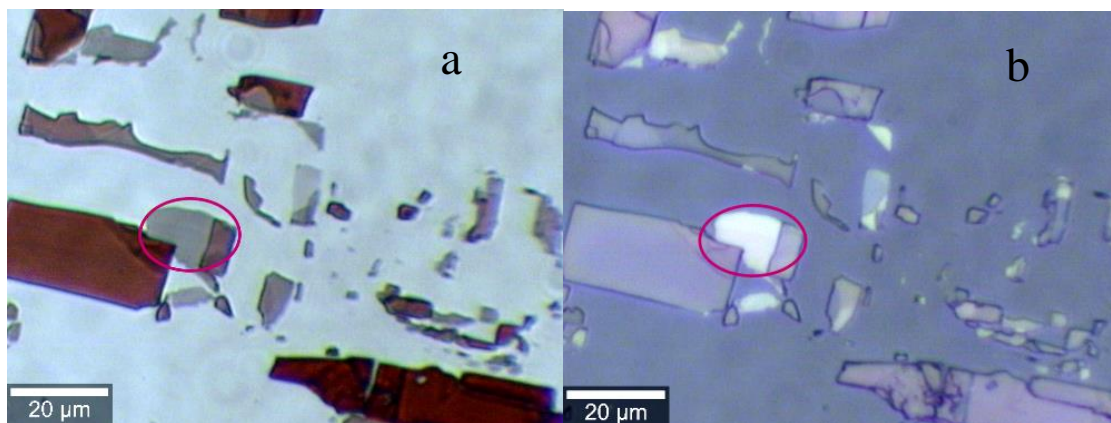


Figure S5. Optical images of the exfoliated crystal a) in transmission light, b) in reflected light.

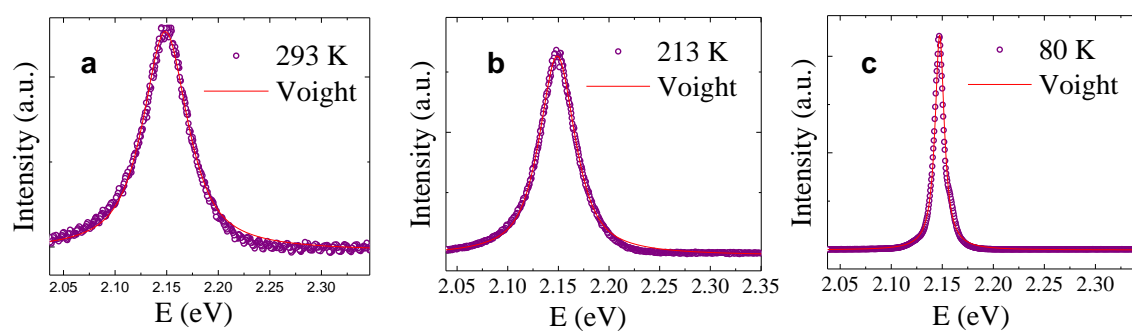


Figure S6. Fitting of PL spectra of $(\text{PEA})_2(\text{MA})[\text{Pb}_2\text{I}_7]$ using one Pseudo-Voigt component.

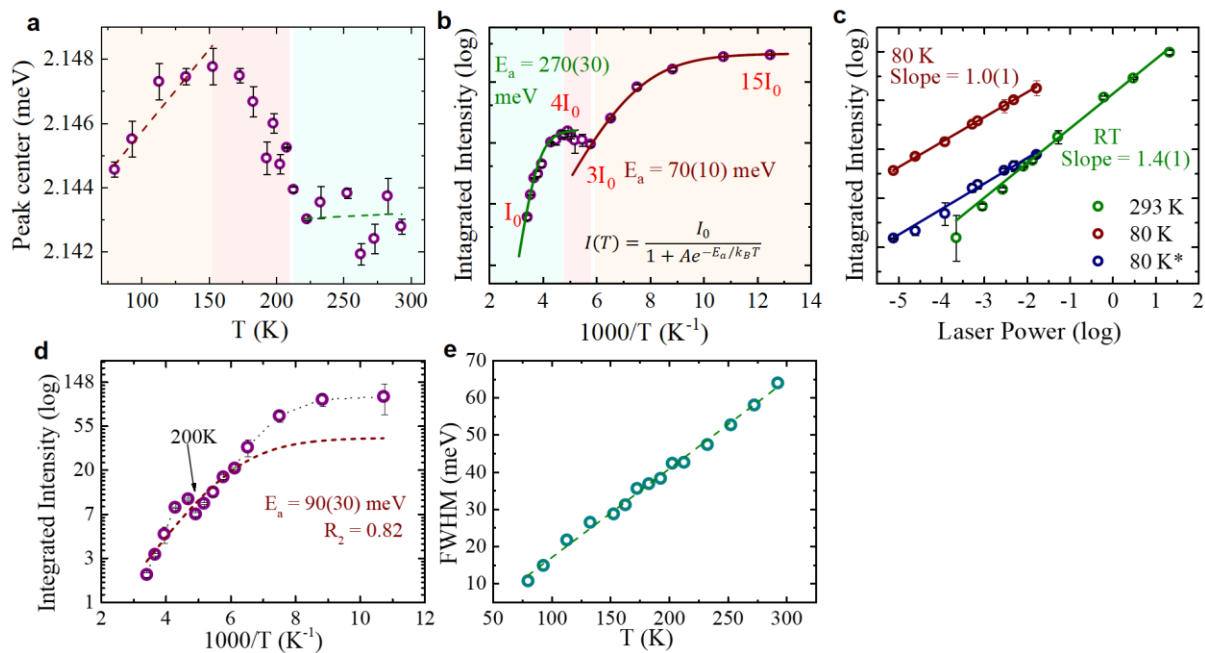


Figure S7. Temperature dependent (heating from 80K to 300 K) PL response under 457 nm excitation showing, (a) PL peak position vs temperature, (b) dependence of integrated PL intensity (logarithmic scale) vs $1/T$ and the fit of these data using $I = I_0 / \left(1 + \exp \left(-\frac{E_a}{k_b T} \right) \right)$, (c) excitation intensity dependence of integrated PL intensity (bilogarithmic scale) vs laser power (green points correspond to RT measurements, brown points represent the main component, blue points represent an additional component at low temperature), (d) integrated PL intensity vs $1/T$ under 457 nm excitation (cooling from 300 to 80K) where a fit of the whole range is presented, (e) full-width-half-maximum (FWHM) of the PL data from the $(\text{PEA})_2(\text{MA})[\text{Pb}_2\text{I}_7]$ systems as a function of temperature.

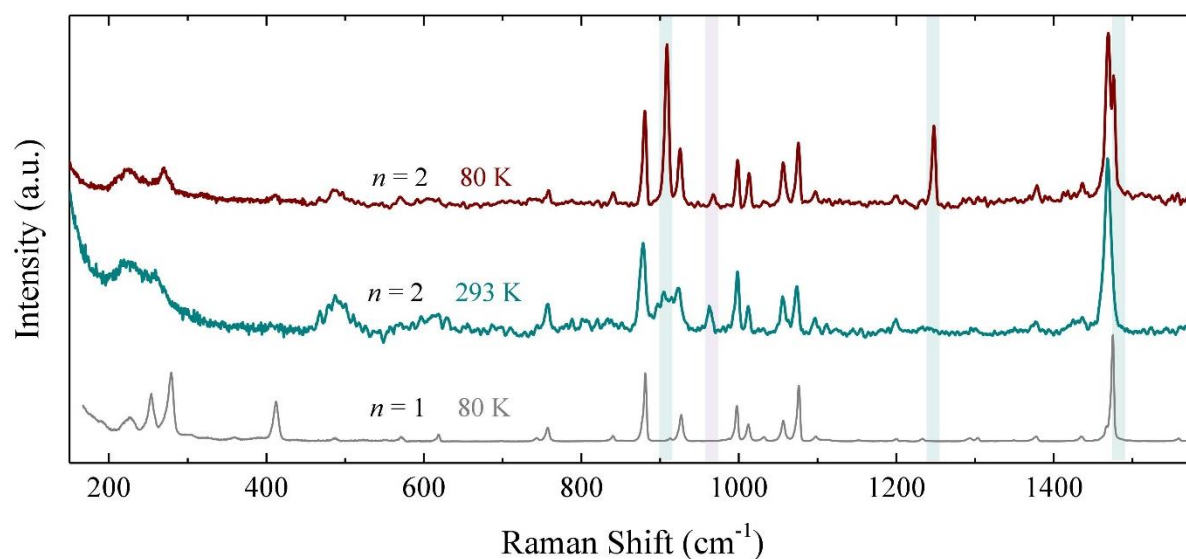


Figure S8. Raman data from $(\text{PEA})_2[\text{PbI}_4]$ ($n = 1$) hybrid perovskite system at 80 K (bottom), and the $(\text{PEA})_2(\text{MA})[\text{Pb}_2\text{I}_7]$ ($n = 2$) system at room temperature and at 80 K. The $(\text{PEA})_2[\text{PbI}_4]$ spectrum is shown for comparison as the framework charge is balanced by PEA^+ cations only. This provides clear evidence that the highlighted peaks appearing in the $(\text{PEA})_2(\text{MA})[\text{Pb}_2\text{I}_7]$ ($n = 2$) spectrum yet absent from the $(\text{PEA})_2[\text{PbI}_4]$ ($n = 1$) spectrum correspond to MA^+ modes. From these data, only the peaks assigned to MA^+ cation vibrations exhibit a strong temperature dependence.

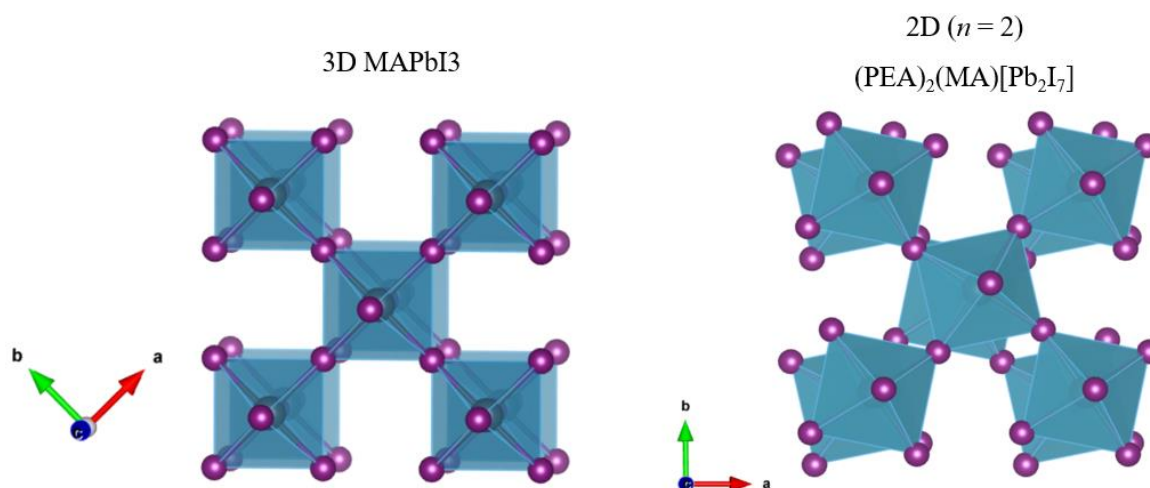


Figure S9. Representations of the inorganic sublattices in 3D (P4mm) and 2D (P1) perovskites.

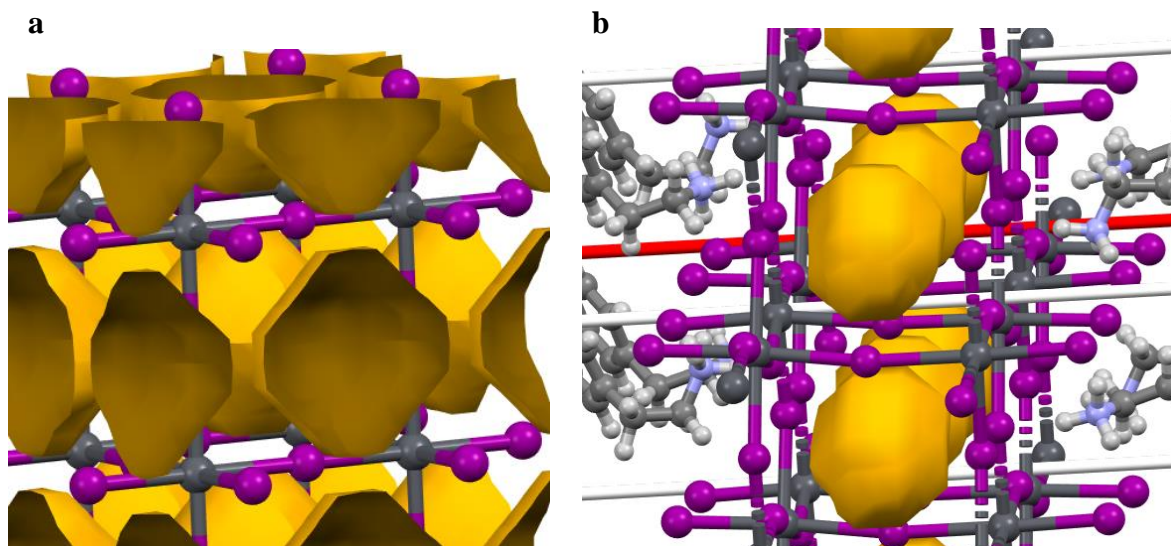


Figure S10. The MA⁺ cavities is a) MAPbI₃ in the tetragonal phase at room temperature (volume = 78.5 Å³), b) in (PEA)₂(MA)[Pb₂I₇] at room temperature (volume = 59.1 Å³). The voids are calculated by means of Mercury software with the following parameters: Probe Radius = 1.8 (MA⁺ ionic radius), Grid Spacing = 0.7.